

# THE ACCELERATOR AND BEAM PHYSICS OF THE MUON $g-2$ EXPERIMENT AT FERMILAB

D. A. Tarazona\*, Cornell University, Ithaca, NY, USA

## Abstract

The physics case of the Muon  $g-2$  Experiment at Fermilab is outstanding and has recently attracted significant attention from its first official results. Although its measurements involve high energy physics methods, such as counting positron production rates with the use of calorimeters and beam diagnostics with tracking detectors, this experiment is strongly bound to accelerator and beam physics. This paper reviews the principles of the experiment and the details necessary to provide a solid ground for the beam-dynamics uncertainties and the corrections of the systematic effects influencing the output of the experiment: a single numerical value, which may unveil new physics.

## INTRODUCTION

The Fermi National Accelerator Laboratory (Fermilab) Muon  $g-2$  Experiment (E989) recently yielded its first measurement of the positive muon magnetic anomaly,  $a_\mu \equiv (g_\mu - 2)/2$ , with an experimental relative uncertainty of 0.46 parts per million (ppm) [1]. This result from the “Run-1” dataset, combined with the previous result from Brookhaven National Laboratory (BNL) [2], differs from the current Standard Model (SM) prediction [3] by 4.2 standard deviations. The error budget of the  $g-2$  experiment (0.14 ppm to strongly establish evidence for new physics) requires the production of a highly polarized muon beam with momentum 3.094 GeV/c and sufficient intensity to collect more than twenty times the number of recorded high-energy positrons from the previous experiment at BNL [4].

In addition, the storage ring is designed to allow for precise measurements and maintain a uniform evolution of the two main frequencies from which  $a_\mu$  is extracted, i.e.,  $a_\mu \propto \omega_a/\tilde{\omega}_p(T_r)$ . The frequency  $\tilde{\omega}_p(T_r)/2\pi \approx 61.7$  MHz is the proton Larmor frequency measured in a spherical water sample at a temperature  $T_r = 34.7^\circ\text{C}$ , weighted by the muon distribution [5]. Such frequency, directly proportional to the magnetic field experienced by the stored muons, regulates the magnitude of the anomalous precession frequency,  $\omega_a/2\pi \approx 0.23$  MHz, which, under design conditions, corresponds to the spin-precession frequency relative to the cyclotron frequency in the laboratory frame [6].

In the following sections, an overview of the accelerator complex at Fermilab, the Muon Campus, for the production and delivery to the storage ring of the muon beam; a description of the main components of the storage ring directly related to the goals of the muon  $g-2$  experiment from the beam dynamics front; and the beam-dynamics systematic corrections in the experimental measurement are presented.

\* dtarazona@cornell.edu

## MUON CAMPUS

The Muon Campus at Fermilab, depicted in Fig. 1, is a series of approximately 1 km-long beamlines between a “pion production” target and the entrance of the Muon  $g-2$  Storage Ring that was designed to meet the statistical goal and deliver  $(0.5-1.0) \times 10^5$  highly polarized muons per  $10^{12}$  protons that arrive at the pion production target [4]. Batches of four/eight

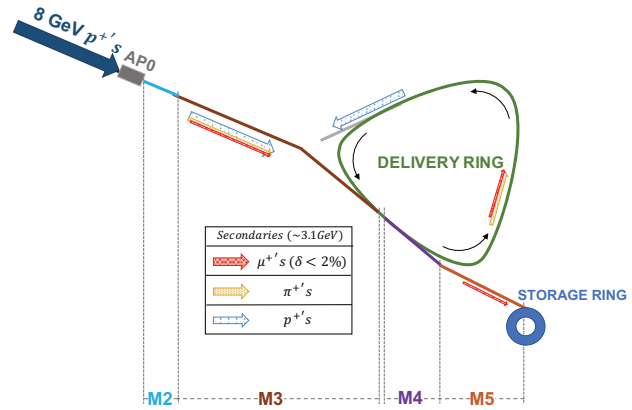


Figure 1: A schematic layout of the Muon Campus [7]. Secondary particles (mostly pions, muons, and protons) downstream of the target station at AP0 are canalized through the M2/M3 lines and injected into the Delivery Ring (DR), where protons are discarded and most of the remaining pions decay after four turns. A beam of mostly muons is extracted to the M4/M5 lines and ultimately delivered to the Muon  $g-2$  Storage Ring.

8.9 GeV/c proton bunches are directed to an Inconel-600 pion production target—an alloy of iron, chromium, and nickel—located at Fermilab’s AP0 target hall from which positive secondary particles emerge. A magnetic quadrupole triplet focuses the proton pulses upstream of the production target to a transverse size of about  $150\ \mu\text{m}$  to minimize beam loss. Mostly pions with momentum acceptance of  $\pm 2\%$  around 3.094 GeV/c are collected and transported along FODO channels, bending magnets, and quadrupole arrangements for dispersion suppression, with an overall transverse acceptance of  $40\pi$  mm.mrad, supported by the beamline apertures of the Muon Campus.

Most of the muon beam emerges via the  $\pi^+ \rightarrow \mu^+ \nu_\mu$  weak-decay channel. As the emitted muons are completely polarized in the pion rest frame and the Muon Campus beamlines impose a stringent momentum acceptance, only highly polarized muons are transported to the storage ring.

MC5: Beam Dynamics and EM Fields

D01: Beam Optics - Lattices, Correction Schemes, Transport

M0PLXGD3

## STORAGE RING

The storage ring is built as one continuous superferric magnet made of mainly six layers of high-quality magnet steel and two pole pieces [5]. Segmented electric quadrupole stations confine the injected muon beam within a toroid of 7.112 m in radius; its circular cross section is defined by five circular collimators, 45 mm in radius, centered around the ideal orbit. Table 1 lists the main parameters that characterize the muon  $g-2$  storage ring, including maximum directional offsets,  $x'$  and  $y'$ , with respect to the optical axis ( $x$  is the radial distance relative to the bending radius and  $y$  is the vertical distance from the midplane of the ring).

Table 1: Storage Ring Representative Parameters

| Parameter                        | Value                   |
|----------------------------------|-------------------------|
| Nominal momentum ( $p_0$ )       | 3.094 GeV/c             |
| Momentum acceptance              | $\pm 0.56\%$            |
| Radial tune ( $\nu_x$ )          | 0.944                   |
| Vertical tune ( $\nu_y$ )        | 0.330                   |
| Bending magnetic field ( $B_0$ ) | 1.4513 T                |
| Bending radius ( $\rho_0$ )      | 7.112 m                 |
| Revolution period                | 149.2 ns                |
| Horizontal admittance            | $268\pi$ mm.mrad        |
| Vertical admittance              | $93\pi$ mm.mrad         |
| Maximum excursion                | 45 mm                   |
| $x'$ max                         | 6 mrad                  |
| $y'$ max                         | 2 mrad                  |
| High-voltage (HV) setpoint       | $\sim \pm 18.3$ kV      |
| Vacuum in storage volume         | $\lesssim 10^{-6}$ Torr |
| Current                          | 5170 A                  |

### Magnetic Field

By design, the magnetic field is intended to be fully oriented in the vertical direction and have a uniform magnitude of  $B_0 = p_0/e\rho_0$ . Magnetic-field temporal stability on the ppm level is required throughout experimental datasets for a precise extraction of the muon magnetic anomaly [5]. On the spatial front, a highly uniform field reduces the uncertainties intrinsic to the determination of the magnetic field experienced by the stored muons.

For this purpose, magnet shimming keeps local variations to less than 50 ppm relative to  $B_0$  (see Fig. 2). With passive

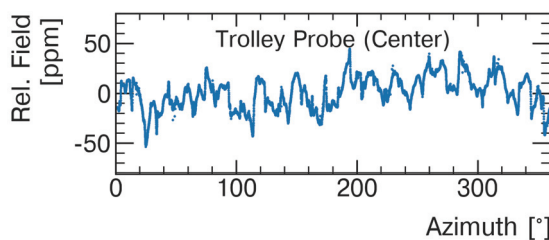


Figure 2: Relative Larmor frequency as measured by a trolley probe across the optical axis, corresponding to magnetic field magnitude variations taken from Run-1 measurements [5].

shimming, pole-pieces positioning drives the overall field strength, whereas additional pieces of iron fine-tune the azimuthally averaged field and control transverse gradients. Moreover, a set of 200 coils installed on each of the upper and lower pole surfaces actively target the azimuthal average of specific multipoles; and the power supply feedback adjusts the supply current to keep the average vertical field constant over time.

The magnetic field is periodically mapped out in the storage region by a mobile set of 17 pulsed nuclear magnetic resonance (NMR) magnetometers distributed across a trolley. Between trolley runs, the field is continuously tracked by  $\sim 380$  NMR probes located above and below the storage region, where field drifts are synchronized with the measurements from the trolley. The signals from free-induction decay signals from the NMR probes provide a  $\sim 10$  ppb-precision measurement of the Larmor precession frequency, which in turn yields the magnetic field at the location of the material sample within the probe. Systematic effects associated with field mapping (e.g., position uncertainties, motion and temperature effects) and field tracking—explained in Ref. [5]—are greatly minimized to the parts-per-billion (ppb) level thanks to the achieved homogeneity of the magnetic field.

### Beam Injection

The optical configuration of the Muon Campus beamlines upstream of the storage ring is meant to focus the beam horizontally for its passage through a backleg hole in the ring, which houses the 18 mm  $\times$  56 mm superconducting inflector magnet [8] meant to cancel out the surrounding magnetic field.

At the inflector exit, the muon beam emerges approximately 77 mm tangentially shifted from the ideal orbit of the storage ring. In order for the injected muons to end up within the ring storage volume, the beam is required to be steered about 10.5 mrad radially outward after a  $\sim 90^\circ$  phase advance. To this end, a fast non-ferric kicker system [9] supplies an integrated magnetic field of 1.1 kG.m oppositely directed to the vertical field of the storage ring. The kicker stations need to pulse at 100 Hz synchronized to the incoming 120 ns muon bunches and shut off before the pulse revolves the 149 ns-long storage ring. In view of these timing specifications, robust pulsers and low-impedance kicker stations are desired to meet the required rise and decay times. From an impedance mismatch, the temporal shapes of the kicker strengths exhibit a ringing structure as the signal is reflected after the main transient field is induced.

Due to the strong focusing for the beam to traverse from the backleg hole to the ring, an optical (and dispersion) mismatch between the storage ring lattice and the Twiss parameters at the inflector exit emerges [10], producing beating as well as coherent betatron oscillations (CBO) of the radial beam centroid, whose amplitude was exacerbated by a suboptimal kicker performance fixed during Run-3. To minimize such effects, application of radio-frequency (RF)

electric fields [11] were incorporated to the ESQ, described next.

### Beam Confinement

The ElectroStatic Quadrupole system (ESQ) is a four-fold azimuthally symmetric system [12] consisting of four stations with two sections. Each quad section has four plates centered around the ideal orbit (see Fig. 3) that provides vertical beam focusing at the cost of horizontal defocusing and nonlinear beam dynamics effects (e.g., CBO decoherence and muon loss rates [13]).

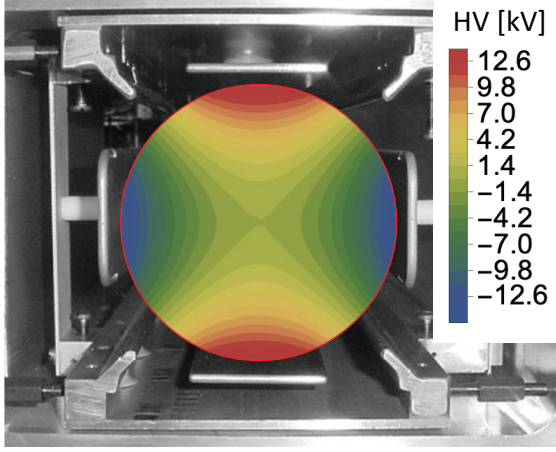


Figure 3: Transverse view of an ESQ station, with an illustration of the main electrostatic potential shown in the storage region (HV= 18.3 kV). The curvature of the plates generates non-linearities, among them a considerable 20 pole that affects mechanical muon loss rates and beam de-coherence.

Each ESQ station consists of a short and long section separated by  $4^\circ$ , and extended by azimuthal lengths of  $13^\circ$  and  $26^\circ$ , respectively. The plates are made with aluminum graded such that their low magnetic susceptibility and thicknesses do not interfere either with the overall magnetic field quality or the positron detection resolution. The four-fold symmetry was chosen to accommodate instrumentation in between the stations and minimize beam variations (i.e., less than 3%) around the ring.

The ESQ plates play the role of electrodes, with circuitry configured to deliver charge for  $700 \mu\text{s}$  in one or two steps. To generate closed orbit distortions for beam scraping purposes, a specific set of plates is connected to 2-step pulsers, which rise initially from 0 to about 6 kV below the nominal high-voltage (HV) setpoint.

### Optical Lattice

The guide fields from the ESQ superimposed over the magnetic field of the storage ring resemble a weak focusing system [14], being the effective field index “ $n$ ” equal to

$$n = -\frac{\rho_0}{vB_0} \frac{\partial E_y}{\partial y} \approx 0.1, \quad (1)$$

where  $E$  denotes the effective electric field along the ideal closed orbit. This approach is sufficient to estimate the

optical lattice functions of the storage ring. However, for more precise calculations to account for azimuthal variations, computational models of the storage ring are developed [15]. Table 2 displays representative values for  $HV = 18.3 \text{ kV}$  from a model of the ring [14] based on COSY INFINITY [16] ( $D$  corresponds to the dispersion function). In this

Table 2: Optical Lattice Representative Parameters

| Parameter  | Value (~)              | Azimuthal Variation    |
|------------|------------------------|------------------------|
| $\alpha_x$ | 0                      | $< \pm 0.1$            |
| $\beta_x$  | 7.5 m                  | $< 3\%$                |
| $\gamma_x$ | $0.13 \text{ m}^{-1}$  | $< 3\%$                |
| $D_x$      | 8 m                    | $< 2\%$                |
| $\alpha_y$ | 0                      | $< \pm 0.2$            |
| $\beta_y$  | 21.5 m                 | $< 3\%$                |
| $\gamma_y$ | $0.046 \text{ m}^{-1}$ | $< 1\%$                |
| $D_y$      | 0.03 m                 | $< \pm 0.01 \text{ m}$ |

model, the high-order structure of the ESQ electrostatic potential beyond the quadrupole term is accounted for via a transverse Taylor expansion [17]. From the magnetic side, the measured ppm-level inhomogeneities are extracted as magnetic multipole strengths from the experimental data.

The main azimuthal modulations of the lattice functions are produced by the segmentation of the ESQ system. Magnetic field imperfections, mostly from the normal quadrupole component, contribute to additional modulations in the optical functions of about 0.5% or less in relation to the case of a perfect magnetic field (see Fig. 4). Since the extracted multipole coefficients from trolley data (except dipole terms) change throughout datasets by less than 100 ppb relative to  $B_0$ , the extra distortions from magnetic field imperfections are not expected to change on a run-by-run basis. Moreover, ESQ plate misalignments can add gradient errors that complicate calculations of the optical lattice. Nevertheless, an external analysis based on alignment survey data determined them to be similar in size to distortions from magnetic field errors. And lastly, less common circumstances might induce time-dependence on the optical lattice, i.e., during Run-1. For this specific case, the lattice parameters were reconstructed from beam diagnostics [18], allowing us to quantify azimuthally dependent effects on the muon weighting of the magnetic field as well as on beam-dynamics systematic corrections.

## BEAM DYNAMICS CORRECTIONS

The anomalous precession frequency  $\omega_a^m$  is measured by exploiting parity violation in the  $\mu^+ \rightarrow e^+ \nu_e \bar{\nu}_\mu$  weak-decay channel. In the muon’s rest frame, a positron with the highest possible energy (i.e., with momentum  $p'_{e \max} \approx 53 \text{ MeV}/c$ ) is produced when the two neutrinos are parallel to each other. On the other hand, parity violation in weak decays constrains the spin and momentum directions of the nearly massless emitted neutrino(anti-neutrino) to be anti-aligned(aligned) (i.e.,  $\pm 1$  helicity). Consequently, conservation of angular momentum implies that the emitted positron fully inherits



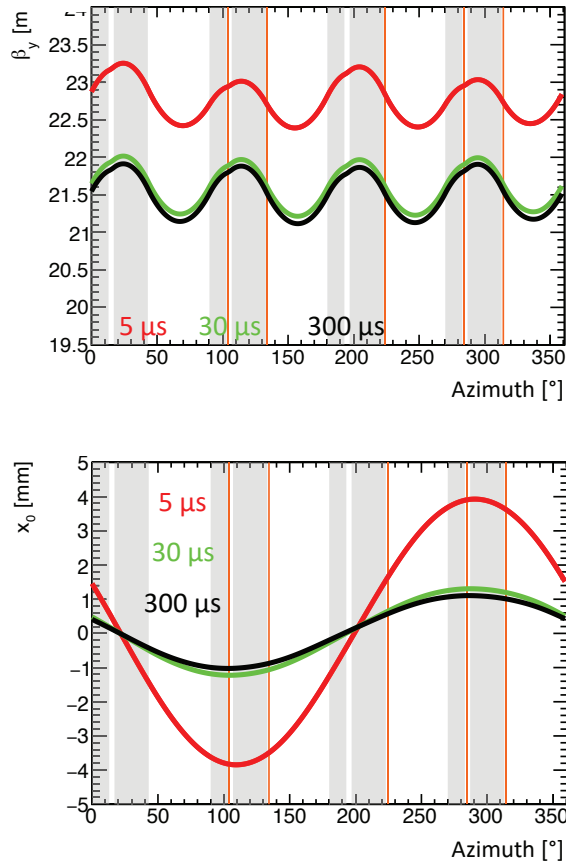


Figure 4: Vertical beta function (top) and radial closed orbits (bottom) versus the ring azimuth for several times after beam injection (HV= 18.3 kV). At 5  $\mu$ s, the lattice is subject to the mis-powered ESQ plates for beam scraping. In particular, vertical and radial closed orbits are distorted to move the beam closer to the collimators (their locations are indicated by vertical orange lines).

the muon's intrinsic angular momentum. Therefore, since the weak interaction couples with the right-handed part of the positron, its emission occurs preferentially in the direction of the muon spin. As such, the number of positrons,  $N(t)$ , emitted with the highest energies in the laboratory frame is modulated over time as

$$N(t) \propto \cos(\omega_a^m t + \varphi_0), \quad (2)$$

where the “ $g$ -2 phase”  $\varphi$  represents the overall angle between spin and momentum of the muon beam at injection time ( $t = 0$ ).

Ideally, polarized muons with “magic momentum”  $p_0 = m_\mu c / \sqrt{a_\mu}$  perfectly injected into the storage ring would circulate around centered orbits of radius  $\rho_0$ , perpendicular to a perfectly uniform vertical magnetic field  $\vec{B}_0$ . Under such circumstances, the frequency at which the muon's spin rotates around the momentum vector in the laboratory frame

would be well defined:

$$\vec{\omega}_a = -a_\mu \frac{e \vec{B}_0}{m_\mu}, \quad (3)$$

where  $e$  is the elementary charge and  $m_\mu$  the muon mass.

However, additional coherent spin precession—either from muons with non-magic momentum or with nonzero vertical betatron motion within the  $\sim 93\pi$  mm.mrad vertical admittance—needs to be accounted for. Moreover, detection effects and correlations between individual  $g$ -2 phases and muon momenta introduce time dependence to the  $g$ -2 phase, potentially biasing the measured precession frequency  $\omega_a^m$ .

These beam dynamics effects are encapsulated as the  $E$ -field ( $C_e$ ), pitch ( $C_p$ ), phase acceptance ( $C_{pa}$ ) and muon loss ( $C_{ml}$ ) corrections. All together, these corrections shift the unbiased frequency:

$$\omega_a \approx \omega_a^m (1 + C_e + C_p + C_{ml} + C_{pa}). \quad (4)$$

For Run-1, the shift was  $(0.50 \pm 0.009)$  ppm; a significant correction to establish disagreements between experimental values and SM predictions of  $a_\mu$ .

From material effects, the acceptance of calorimeters to detect positrons depends on the transverse location of the muon from which they decayed. This feature originates additional modulations in Eq. 2 caused by the CBO of the beam [6]. Even though amplitude- and momentum-dependent betatron tune shifts—strongly driven by the 20 pole of the ESQ electrostatic potential [19]—damp the amplitudes of coherent beam transverse motion on scales of 200  $\mu$ s, the de-coherence modeling introduces a systematic error that is greatly reduced by the recent implementation of ESQ RF electric fields mentioned above.

The distinctive features of the beam dynamics corrections are described next.

### *E-field and Pitch Corrections*

The  $E$ -field and pitch corrections are used to counteract the additional spin precessions due to the momentum spread and vertical betatron motion of the beam, respectively. The standard expressions [15] to quantify them are

$$C_e = \frac{n\beta^2}{1-n} 2 \langle \delta^2 \rangle, \quad C_p = \frac{n}{2\rho_0^2} \langle y^2 \rangle, \quad (5)$$

where  $n$  is the field index,  $\beta$  the normalized velocity of the muon,  $\delta$  is the fractional momentum offset relative to  $p_0$ , and the angle brackets denote average over the stored muons. These expressions are derived from the T-BMT equation [20], wherein  $C_e$  is the lowest-order term from interactions of off-momentum muons with the quadrupole term of the ESQ, and  $C_p$  arises mostly from the vertical betatron frequency induced by the same electric field, provided  $\omega_y \gg \omega_a$  [21]. Both expressions in Eq. 5 have been tested in tracking simulations under realistic scenarios (i.e., segmented ESQ plates, non-linearities, and ESQ plate mis-alignment), proving them to be accurate for the experiment purposes.

The momentum spread has to be measured in order to calculate the E-field correction. For this purpose, special methods (e.g., Fourier transforms [22]) reconstruct the momentum spread out of the cyclotron frequencies that determine the structure of the beam intensity signal detected by calorimeters (see Fig. 5). The systematic uncertainty of  $C_e$

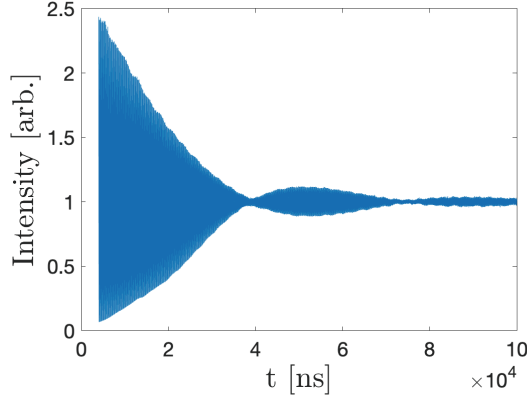


Figure 5: Sample of an intensity signal measured by calorimeters. Beam modulations from  $\omega_a$  and the exponential decay are factored out of the signal.

is dominated by the correlation between momentum and the time-of-flight of muons posterior to the injection kick; asymmetries are consequently introduced to the intensity signal, for which additional methods are developed to account for these effects [15].

For the pitch correction, the vertical beam profile is measured by the straw tracker detectors [23]. As positrons ionize argon gas inside layers of 5 mm-thick straws along their paths, a fitting algorithm extrapolates the muon decay positions. Associated systematic errors are dominated by tracking reconstruction and ESQ voltage errors.

### Phase-drift Corrections

Both the phase acceptance and muon loss corrections shift  $\omega_a^m$  by inducing time dependence on the  $g-2$  phase over the data taking period (i.e.,  $> 30 \mu\text{s}$  after injection).

The phase acceptance correction  $C_{pa}$  accounts for phase changes from the detection side. From the parity-violating muon decay  $\mu^+ \rightarrow e^+ \nu_e \bar{\nu}_\mu$ , highest energy positrons are emitted in the muon spin direction with a probability proportional to the angle between these two directions. In addition, the positron emitted direction together with its energy and initial transverse coordinates in the storage volume determine whether it is detected by a calorimeter or not. Therefore, since the  $g-2$  phase carried by a positron is indirectly related to its initial direction due to the parity-violating decay process, positron transverse decay coordinates and  $g-2$  phases are correlated. Phase acceptance maps in transverse  $x-y$  planes along the storage region are prepared with a *Geant4*-based simulation program named *gm2ringsim* [24]. The model includes decay modules as well as all of the active detectors and most of the passive components installed in the

storage ring, which allows high-detail modeling of material effects that emitted positrons experience. Figure 6 shows a typical phase-acceptance map prepared with the *gm2ringsim* model.

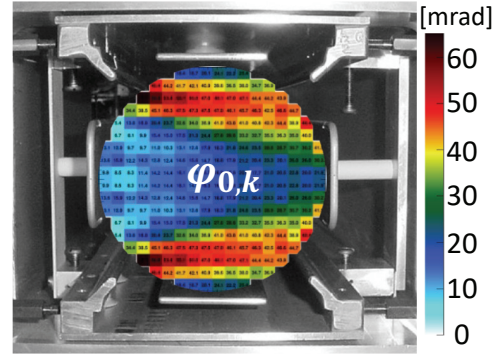


Figure 6: Typical detected-phase acceptance map from *gm2ringsim*. Values indicated by the color legend (in mrad) are relative to a central  $g-2$  phase defined at injection.  $1 \mu\text{rad}$  phase shifts over a muon lifetime in the laboratory frame induce  $\omega_a$  shifts of about 10 ppb.

Lastly, a correlation between momentum and the  $g-2$  phase of about  $-10.0 \pm 1.6 \text{ mrad per } \delta = 1\%$  builds up from the muon beam revolving in the Delivery Ring at the Muon Campus. When muons within specific momentum subranges inside the ring's momentum acceptance are lost due to mechanical interactions, the  $g-2$  phase can change over the data taking period. For Run-1, mechanical muon loss rates exacerbated by the betatron resonance condition  $3\nu_y = 1$  produced a correction of  $(-11 \pm 5 \text{ ppb})$  [15].

## CONCLUSION

A combination of beam preparation, injection, collimation, and storage provides the means to prepare the muon beam from which the muon magnetic anomaly is measured to the precision level required for the experimental goal. The highly uniform magnetic field, as well as an electric focusing system that contributes minimally to beam azimuthal variations, allows for a uniform evolution of the muons' spin precession and cyclotron frequencies. Momentum spread and vertical betatron motion introduce additional spin dynamics. Also, detection effects and mechanical muon losses bias the measured anomalous precession frequency. With well-established beam dynamics corrections supported by sophisticated detection systems, methods, and beam dynamics simulations, such effects are quantified and applied to the experimental measurements.

## ACKNOWLEDGEMENTS

The work was supported by the Fermi Research Alliance, LLC under Contract No. DE-AC02-07CH11359 with the U.S. Department of Energy, Office of Science, Office of High Energy Physics.

## REFERENCES

- [1] B. Abi *et al.* (Muon  $g-2$  Collaboration), “Measurement of the Positive Muon Anomalous Magnetic Moment to 0.46 ppm,” *Phys. Rev. Lett.*, Vol. 126, 141801 (2021).  
doi:10.1103/PhysRevLett.126.141801
- [2] G. W. Bennett *et al.* (Muon  $g-2$  Collaboration), “Final report of the muon E821 anomalous magnetic moment measurement at BNL,” *Phys. Rev. D*, Vol. 73, 072003 (2006).  
doi:10.1103/PhysRevD.73.072003
- [3] T. Aoyama *et al.*, “The anomalous magnetic moment of the muon in the standard model,” *Phys. Rep.*, Vol. 887, 1 (2020).  
doi:10.1016/j.physrep.2020.07.006
- [4] D. Stratakis *et al.*, “Commissioning and first results of the Fermilab Muon Campus,” *Phys. Rev. Accel. Beams*, Vol. 22, 011001 (2019).  
doi:10.1103/PhysRevAccelBeams.22.011001
- [5] T. Albahri *et al.* (Muon  $g-2$  Collaboration), “Magnetic-field measurement and analysis for the Muon  $g-2$  Experiment at Fermilab,” *Phys. Rev. A*, Vol. 103, 042208 (2021).  
doi:10.1103/PhysRevA.103.042208
- [6] T. Albahri *et al.* (Muon  $g-2$  Collaboration), “Measurement of the anomalous precession frequency of the muon in the Fermilab Muon  $g-2$  Experiment at Fermilab,” *Phys. Rev. D*, Vol. 103, 072002 (2021).  
doi:10.1103/PhysRevD.103.072002
- [7] D. A. Tarazona *et al.*, “Dynamical simulations of the Muon Campus at Fermilab,” *Int. J. Mod. Phys. A*, Vol. 34, No. 36, 1942033 (2019).  
doi:10.1142/S0217751X19420338
- [8] A. Yamamoto *et al.*, “The superconducting inflector for the BNL  $g-2$  Experiment,” *Nucl. Instrum. Methods Phys. Res., Sect. A*, Vol. 491, 23 (2002).  
doi:10.1016/S0168-9002(02)01232-9
- [9] A. P. Schreckenberger *et al.*, “The fast non-ferric kicker system for the Muon  $g-2$  Experiment at Fermilab,” *Nucl. Instrum. Methods Phys. Res., Sect. A*, Vol. 1011, 165597 (2021).  
doi:10.1016/j.nima.2021.165597
- [10] D. Rubin *et al.*, “Muon beam dynamics and spin dynamics in the  $g-2$  storage ring,” in *Proc. 9th Int. Particle Accelerator Conf. (IPAC'18)*, Vancouver, BC, Canada, May 2018, pp. 5029-5034.  
doi:10.18429/JACoW-IPAC2018-FRXGBE2
- [11] O. Kim *et al.*, “Reduction of coherent betatron oscillations in a muon  $g-2$  storage ring experiment using RF fields,” *New J. Phys.*, Vol. 22, 063002 (2020).  
doi:10.1088/1367-2630/ab83d0
- [12] Y. K. Semertzidis *et al.*, “The Brookhaven muon ( $g-2$ ) storage ring high voltage quadrupoles,” *Nucl. Instrum. Methods Phys. Res., Sect. A*, Vol. 503, 458 (2003).  
doi:10.1016/S0168-9002(03)00999-9
- [13] D. A. Tarazona, M. Berz, and K. Makino, “Muon loss rates from betatron resonances at the Muon  $g-2$  storage ring at Fermilab,” *Int. J. Mod. Phys. A*, Vol. 34, 1942008 (2019).  
doi:10.1142/S0217751X19420089
- [14] D. A. Tarazona, “Beam Dynamics Characterization and Uncertainties in the Muon  $g-2$  Experiment at Fermilab,” PhD Thesis, Michigan State University (2021).  
doi:10.25335/8ssr-p866
- [15] T. Albahri *et al.* (Muon  $g-2$  Collaboration), “Beam dynamics corrections to the Run-1 measurement of the muon anomalous magnetic moment at Fermilab,” *Phys. Rev. Accel. Beams*, Vol. 24, 044002 (2021).  
doi:10.1103/PhysRevAccelBeams.24.044002
- [16] K. Makino and M. Berz, “COSY INFINITY Version 9,” *Nucl. Instrum. Methods Phys. Res., Sect. A*, Vol. 558, No. 1, p. 346 (2006).  
doi:10.1016/j.nima.2005.11.109
- [17] E. Valetov, “Computation of the main and fringe fields for the electrostatic quadrupoles of the Muon  $g-2$  storage ring,” *Int. J. Mod. Phys. A*, Vol. 34, No. 36, 1942041 (2019).  
doi:10.1142/S0217751X19420417
- [18] D. A. Tarazona *et al.*, “Beam-based diagnostics of electric guide fields and lattice parameters for Run-1 of the Muon  $g-2$  Storage Ring at Fermilab,” presented at the 13th International Particle Accelerator Conf. (IPAC'22), Bangkok, Thailand, Jun. 2022, paper MOPOTK035, this conference.
- [19] A. Weisskopf, D. A. Tarazona, and M. Berz, “Computation and consequences of high order amplitude- and parameter-dependent tune shifts in storage rings for high precision measurements,” *Int. J. Mod. Phys. A*, Vol. 34, No. 36, 1942011 (2019).  
doi:10.1142/S0217751X19420119
- [20] V. Bargmann, L. Michel, and V. L. Telegdi, “Precession of the polarization of particles moving in a homogeneous electromagnetic field,” *Phys. Rev. Lett.*, Vol. 2(10), 435 (1959).  
doi:10.1103/PhysRevLett.2.435
- [21] O. Kim, “Analytical estimations of the chromaticity and corrections to the spin precession frequency in weak focusing magnetic storage rings,” *Phys. Rev. Accel. Beams*, Vol. 25, 024001 (2022).  
doi:10.1103/PhysRevAccelBeams.25.024001
- [22] Y. Orlov, C. S. Ozben, and Y. K. Semertzidis, “Muon revolution frequency distribution from a partial-time Fourier transform of the  $g-2$  signal in the muon  $g-2$  experiment,” *Nucl. Instrum. Methods Phys. Res., Sect. A*, Vol. 482(3), 767 (2002).  
doi:10.1016/S0168-9002(01)01703-X
- [23] B.T. King *et al.*, “The straw tracking detector for the Fermilab Muon  $g-2$  Experiment,” *J. Instrum.*, Vol. 17, 02035 (2022).  
doi:10.1088/1748-0221/17/02/p02035
- [24] T. Arvanitis and A. Lyon, “artG4: A Generic Framework for Geant4 Simulations,” in *J. Phys. Conf. Ser.*, Vol. 513, 022023 (2014).  
doi:10.1088/1742-6596/513/2/022023